ORIGINAL PAPER

Evaluation of the WRF model for a heavy rainfall event over the complex mountainous topography of Mandi, India

Sourabh Garg[1,4] · Gaurav Tiwari[2,3] · Sarita Azad[1]

Abstract

Cumulus convection clouds can produce a lot of rain in a short duration of time over a constrained area. Severe natural disasters like cloudbursts are regularly experienced as heavy rainfall events (HREs) in the North-West Himalayan region and during the Indian Summer Monsoon Rainfall season (June–September). These events cause significant losses in terms of life, infrastructure, crops, etc. Therefore, it is crucial to understand and predict such events in order to minimize costs. This study simulates an HRE that occurred in Mandi, India, on August 7, 2015, for a period of 24 h using the Weather Research and Forecasting (WRF) model, a numerical weather prediction system. To study the key elements of HRE, various cloud microphysics (CMP) methods are subjected to a sensitivity analysis. Ten CMP systems (CAM, Goddard, Lin, Milbrandt-Yau, Morrison, Thompson, WDM6, WSM3, WSM5, and WSM6) are taken into account in the sensitivity analysis. To ascertain how well the WRF model with each scheme represents such extreme localized heavy rainfall episodes, the model output is examined. The Indian Monsoon Data Assimilation and Analysis (IMDAA) reanalysis and the Integrated Multi-satellitE Retrievals for Global Precipitation Measurement (GPMIMERG) Final run (V06B) satellite estimate datasets are used to create the observation proxies, which have horizontal resolutions of 12 km and 10 km, respectively. The output examination of the coarser and higher resolutions revealed that the WSM3 method performed very closely to the observation. Additionally, the bias in the simulated rainfall distributions of the Morrison and WSM3 schemes is evaluated for both domains; the WSM5 schemes showed the least error. Several meteorological variables that are connected to rainfall patterns, such as cloud fraction, maximum reflectivity, convective available potential energy, and wind flow field, are also thoroughly examined.

Keywords WRF model · Heavy rainfall event · Himalayas · Parameterization schemes

✉ Sarita Azad
  sarita@iitmandi.ac.in

1   School of Mathematical and Statistical Sciences, Indian Institute of Technology Mandi, Mandi, India

2   Department of Earth and Environmental Sciences, Indian Institute of Science Education and Research Bhopal, Bhopal, India

3   Department of Global Environment and Disaster Prevention Sciences, Hirosaki University, Hirosaki, Japan

4   School of Basic Sciences, Galgotias University, Greater Noida, India

1 Introduction

The Himalayas in northern India significantly influence the meteorological patterns (weather and climate) of the Indian subcontinent. The severe weather phenomena and extreme events such as Heavy Rainfall Events (HREs) in the northern states of India, including Jammu and Kashmir, Himachal Pradesh, and Uttarakhand, are primarily influenced by their complex topography (Dimri et al. 2017; Bharti 2015; Shekhar et al. 2010). Seasonal winds that reverse their direction and cause precipitation are monsoon winds (Rajeevan et al. 2012; Ramage 1971). The Indian summer monsoon rainfall season comes with probably the most complex air-sea interaction circulation system globally. It mainly affects India and its surrounding regions and brings a lot of rain from June to September. It is also called the southwest monsoon season (Vellore et al. 2016; Rajeevan et al. 2012; Raju et al. 2005; Raghavan 1973). The Indian summer monsoon has different types of rain, whether onset and retrieve, active spell or break (Raju et al. 2005). Before the southwesterly monsoon circulation starts, intense spring heating causes a thermal low across the northern Indian subcontinent. Due to the high altitude of the Himalayan ranges, India's wind circulation patterns change during June and July (Singh and Mal 2014). Because of the lifting through the mountain slopes, the circulation overturns, causing the moisture content in the air mass to increase. Heavy precipitation occurs in that area when an air mass with enough moisture to precipitate saturates at a specific level. Because of the interplay of monsoon currents with the slopes, most rain falls in the valleys.

In the Shivalik foothills along the Beas River, Mandi (31.7°N, 76.7°E) is located in the heart of Himachal Pradesh, surrounded by high mountains and deep terrains with significant moisture content. The HRE refers to a confined meteorological event that lasts a few hours and occurs in a narrow section (less than 20–30 square kilometers). As a result of these calamities, flash floods, landslides, home collapses, transportation disruptions, and human fatalities occur. Cumulus convective clouds grow over a given area and have the potential to deliver a large amount of rain in a short period. Cumulonimbus convection is described as a result of steep orography and moisture-induced thermodynamic instability (Das et al. 2006). On August 04 and August 08 of 2010, similar incidents occurred over Mandi at roughly 0300 and 0400 UTC. Heavy downpour water caused landslides and flash floods, resulting in the deaths of five persons and the destruction of 44 houses and 82 cowsheds (Dimri et al. 2017; Jena et al. 2020). Many people lost their lives and possessions because the incident occurred at midnight. Cattle and automobiles were washed away in great numbers. During the monsoon season, cloudbursts are common in the NWH region, resulting in severe downpours of up to 100 mm/hr. The orography of the locations simulates the convective process, resulting in severe cloudbursts. The WRF model provides a wide range of the study of meteorological applications (Kumar et al. 2017; Tiwari et al. 2019, 2022; Tiwari and Kumar 2022, 2023). Several studies with the WRF model have been done over the NWH region, as shown in Table 1.

In the present study, an HRE over the Mandi (India) is considered for the high-resolution WRF model simulations on August 07 2015 (https://www.downtoearth.org.in/). It had caused flash floods and heavy landslides, due to which loss of lives and property were faced. INSAT-3D multispectral daily rainfall from the Meteorological Satellite Data Archival Center (MOSDAC) of Space Applications Center (SAC), India valid for 05:30 Indian Standard Time on 07 August 2015 over the Mandi region is shown in

Table 1 The literature for HRE events study using the WRF model over India

S. No	References	Parameterization schemes	Domain	Datasets	Region
1	Chevuturi et al. (2015)	WSM6	3 domains (27 km, 9 km, 3 km)	TMPA 3B42 V7, station data	Rudraprayag, Uttarakhand
2	Devi et al. (2021)	WSM6	Single domain (9 km)	SASE observation	Jammu & Kashmir, Himachal Pradesh
3	Karki et al. (2017)	Morrison	3 domain (25 km, 5 km, 1 km)	29 meteorological stations	Nepal Mountainous region
4	Karki et al. (2018)	Thompson	Single domain (4 km)	TRMM 3B42, GPM, MODIS, Gauge observation	Nepal Mountainous region
5	Khadke and Pattnaik (2021)	Milbrandt-Yau, Thompson, WDM6, Aerosol aware Thompson	2 domains (9 km, 3 km)	ECMWF-ERA5, NCEP-FNL, ERA5 Reanalysis RANA, IMD	Kerala
6	Mohan and Bhati (2011)	Pleim-Xiu land surface model, Pleim surface layer scheme, and Asymmetric Convective Mode	3 domains (27 km, 9 km, 3 km)	Station data	Delhi
7	Patil and Pradeep Kumar (2016)	WSM3, WSM5, Eta, SBU-YLin, NSSL 1-moment	3 domains (81 km, 27 km, 9 km)	IMD	Northwestern Himalayan region
8	Pegahfar et al. (2022)	Lin	2 domains (27 km, 9 km)	GPM (Late run), Meteorological stations, Iran Meteorological Organization (IRIMO)	Pol-Dokhtar, Iran
9	Sravana Kumar et al. (2012)	WSM3, WSM6	4 domains (81 km, 27 km, 9 km, 3 km)	TRMM	Leh, Jammu & Kashmir

Fig. 1 INSAT-3D multispectral daily rainfall from the Meteorological Satellite Data Archival Center (MOSDAC) of Space Applications Center (SAC), India valid for 05:30 Indian Standard Time on 07 August 2015
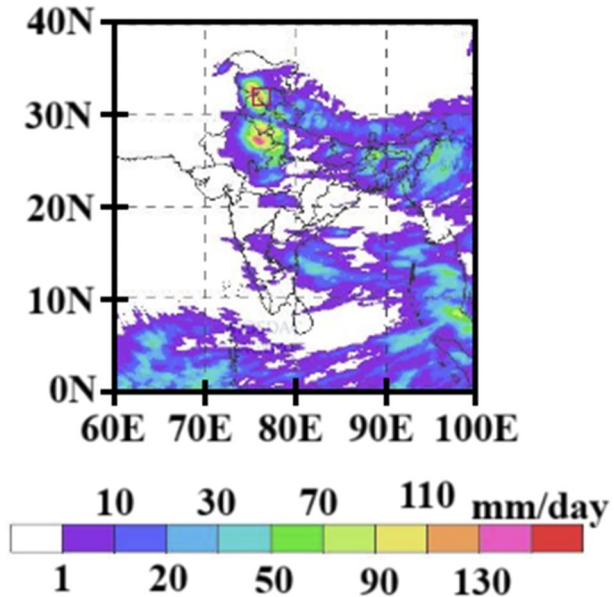

Fig. 1. The model set-up was customized with two domains (outer and inner) with horizontal resolutions of 27 and 9 km, respectively, and experiments were performed for ten cloud microphysics schemes.

2 Model framework and experimental design

2.1 Model description

The non-hydrostatic Advanced Research WRF model developed by the National Center for Atmospheric Research (NCAR) (Skamarock et al. 2019) is used in the study. Table 2 shows the detailed configuration of WRF model version 3.8 used in this study. The model was set up with two nested domains with a resolution of 27 km (outer domain) and 9 km (inner domain). Figure 2 depicts these domains' size and the second domain's topography. The simulations were carried out on August 07 2015, over 24 h. A total of ten experiments were conducted for ten cloud microphysics (CMPs) (Table 3).

The initial and boundary conditions for the model integration were taken from the high-resolution Global Forecast System (GFS) with $0.25° \times 0.25°$ spatial resolution and 6-h temporal resolution from the National Centers for Environmental Prediction-Global Data Assimilation System (NCEP-GDAS) and NCEP-Final (NCEP-FNL). The IMDAA reanalysis dataset (Ashrit et al. 2020, https://rds.ncmrwf.gov.in/) and the GPM IMERG (Final run) satellite estimate (Huffman et al. 2019, https://gpm.nasa.gov/data/directory) are being used to validate the model.

Table 2 Description of the WRF model configuration used in the study

Description of the WRF model configuration	
Model type	Primitive equation, non-hydrostatic; dynamic core; Eulerian mass coordinate
Vertical resolution	27 sigma levels
Duration of simulation	August 07 2015 (24 h)
Horizontal grid system	Arakawa C grid staggering
Horizontal grid resolution	27 km (1st domain), 9 km (2nd domain)
Acoustic and gravity wave model	3rd order Runge–Kutta scheme
Time step	120 s
Central point of the domain	$31.7°N$, $76.7°E$ (Mandi)
Domain of integration	Parent domain $(10 − 43°N, 55 − 110°E)$
	Inner domain $(20 − 38°N, 65 − 100°E)$
Radiation schemes	Longwave radiation (LWR): Rapid radiative transfer model (RRTM) (Mlawer et al. 1997)
	Shortwave radiation (SWR): Dudhia scheme (Dudhia 1989)
Surface Physics	Revised MM5 scheme (Jiménez et al. 2012)
Land surface	Unified Noah land surface model (Tewari et al. 2004)
Planetary boundary layer (PBL) scheme	Yonsei University scheme (YSU) (Hong et al. 2006)
Cumulus parameterization (CP) scheme	Kain-Fritsch (KF) scheme (Kain 2004)
Cloud microphysics (CMP) scheme	CAM V5.1 2-moment 5-class scheme (Eaton 2011)
	Goddard scheme (Tao et al. 1989, 2016)
	Purdue Lin scheme (Chen and Sun 2002)
	Milbrandt-Yau Double Moment scheme (Milbrandt and Yau 2005a, 2005b)
	Morrison 2-moment scheme (Morrison et al. 2009)
	Thompson scheme (Thompson et al. 2008)
	WRF Double Moment 6-class scheme (WDM6) (Lim and Hong 2010)
	WRF Single Moment 3-class scheme (WSM3) (Hong et al. 2004)
	WRF Single Moment 5-class scheme (WSM5) (Hong et al. 2004)
	WRF Single Moment 6-class scheme (WSM6) (Hong and Lim 2006)
Map projection	Mercator
Initial and boundary conditions	National Centers for Environmental Prediction's (NCEP) FNL

2.2 Experimental design

WRF cloud microphysics schemes are used, each with its own set of possibilities, and sensitivity experiments have been carried out (shown in Tables 2 and 3) while the other parameterization options are fixed. The brief details about selected CMPs are provided below:

2.2.1 CAM V5.1 double moment 5-class scheme

It is the most recent of a series of global atmospheric models developed. It is a double moment 5-class scheme (Eaton 2011), which predicts ice snow graupel.
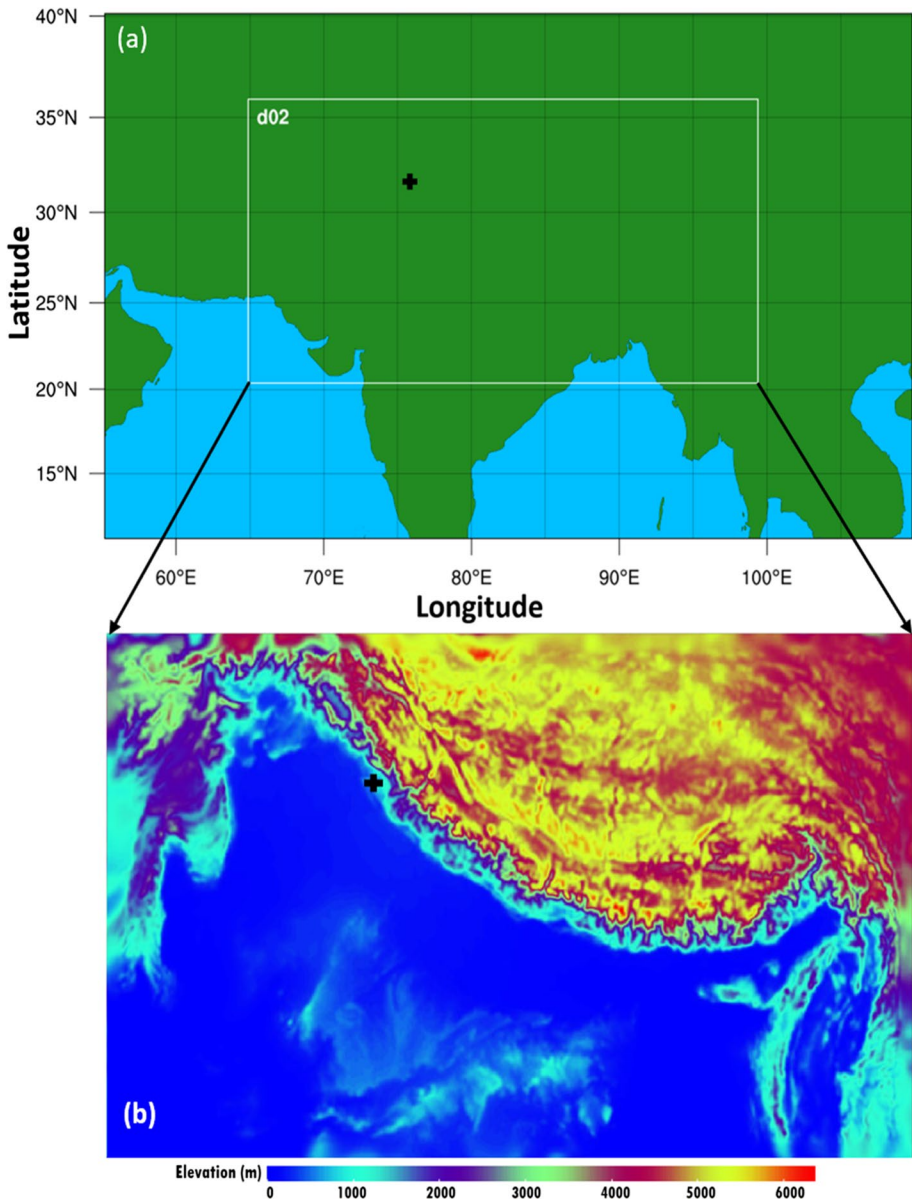
Fig. 2 **a** Model domains in which two boxes indicate outer and inner domains with a horizontal resolution of 27- and 9-km, respectively. The detailed topography of the inner domain is shown in (**b**). The plus sign represents the location of the Mandi region (31.7°N, 76.7°E)

2.2.2 Goddard scheme

It predicts hail and graupel separately and provides effective radii for radiation (Tao et al. 1989, 2016).

Table 3 Description of the numerical experiments performed in the study by using various cloud microphysics schemes

Experiment	CMP	CP	PBL	LWR	SWR
1	CAM	KF	YSU	RRTM	Dudhia
2	Goddard				
3	Lin				
4	Milbrandt-Yau				
5	Morrison				
6	Thompson				
7	WDM6				
8	WSM3				
9	WSM5				
10	WSM6				

2.2.3 Purdue Lin scheme

It is a sophisticated scheme with ice, snow and graupel processes, suitable for real-data high-resolution simulations (Chen and Sun 2002).

2.2.4 Milbrandt-Yau double moment 7-class scheme

With the double-moment cloud, rain, ice, snow, graupel, and hail, the Milbrandt-Yau double-moment 7-class scheme (Milbrandt and Yau 2005a, 2005b) gives separate categories for hail and graupel.

2.2.5 Morrison double moment scheme

It is a double-moment scheme which predicts ice, snow, rain, and graupel for cloud-resolving simulations (Morrison et al. 2009).

2.2.6 Thompson scheme

In addition, the Thompson scheme (Thompson et al. 2008) is similar to WSM6, but it includes a more accurate saturation adjustment scheme and improved snow and graupel collection (Thompson et al. 2004).

2.2.7 WRF double moment 6-class scheme (WDM6)

This scheme (Lim and Hong 2010) has double-moment rain, ice, snow, and graupel processes suitable for high-resolution simulations. It also predicts cloud and cloud condensation nuclei (CCN) for warm processes, unlike WSM6.

2.2.8 WRF single moment 3-class scheme (WSM3)

It is a simple, efficient scheme with ice and snow processes suitable for mesoscale grid sizes (Hong et al. 2004).

2.2.9 WRF single moment 5-class scheme (WSM5)

It is a slightly more sophisticated version of WSM3 that allows for mixed-phase processes and super-cooled water (Hong et al. 2004).

2.2.10 WRF single moment 6-class scheme (WSM6)

It is a simple and efficient scheme with ice, snow, and graupel processes for high-resolution grid sizes (Hong and Lim 2006). WSM6 is also the best choice for cloud-resolving grids due to its efficiency and theoretical foundation.
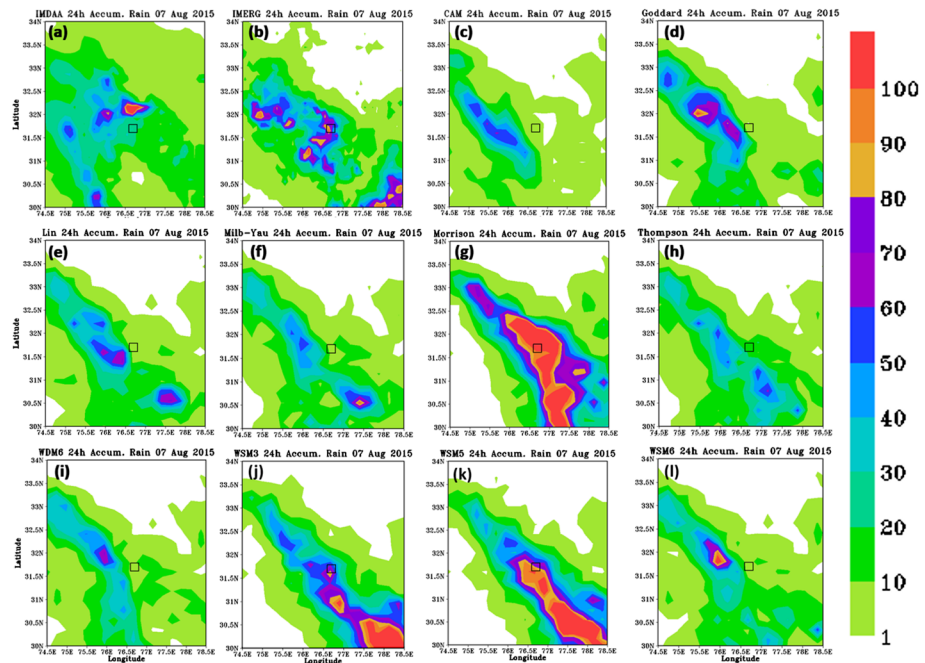
Fig. 3 Accumulated precipitation (mm/day) of the outer domain (1st) valid for 24 h during August 07 2015 from observations **a** IMDAA, **b** satellite estimate GPM IMERG (Final run), and from model outputs with different parameterization schemes, i.e., **c** CAM, **d** Goddard, **e** Lin, **f** Milbrandt-Yau, **g** Morrison, **h** Thompson, **i** WDM6, **j** WSM3, **k** WSM5, and **l** WSM6. The box symbol represents the location of the Mandi (31.7°N, 76.7°E) region
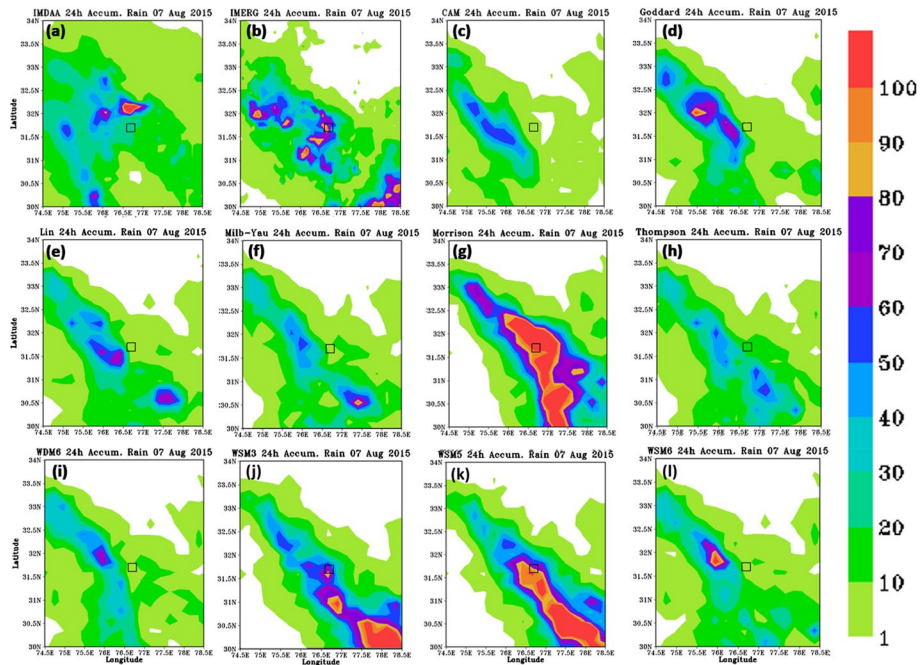
Fig. 4 Accumulated precipitation (mm/day) of the inner domain valid for 24 h during August 07 2015 from observations **a** IMDAA, **b** satellite estimate GPM IMERG (Final run), and from model outputs with different parameterization schemes, i.e., **c** CAM, **d** Goddard, **e** Lin, **f** Milbrandt-Yau, **g** Morrison, **h** Thompson, **i** WDM3, **j** WSM3, **k** WSM5, and **l** WSM6. The box symbol represents the location of the Mandi (31.7°N, 76.7°E) region

3 Results

3.1 Comparison of the simulated rainfall for outer and inner domains

The model outputs for the HRE over the Mandi region are computed given two reanalysis products as the proxy for observation, namely IMDAA and GPM IMERG for the outer and inner domains, as shown in Figs. 3 and 4. We consider the HRE that happened across the study region for 24 h (1 day) on August 7, 2015. In this case, IMDAA revealed less precipitation (approx. 21.83 mm/day) across the study area (Figs. 3a and 4a). GPM IMERG detected heavier rainfall/precipitation (104.82 mm/day) than IMDAA, as seen in Figs. 3b and 4b. As a result, we can use GPM IMERG as a basis for comparison from observations.

The simulation with the Morrison scheme is the best match with GPM IMERG in the outer domain (Fig. 3), closely followed by the WSM5 and WSM3 schemes over the study region. The Morrison, WSM5, and WSM3 schemes spatially overestimated the IMDAA and GPM IMERG. When dealing with higher resolution for the inner domain (as illustrated in Fig. 4), WSM3 spatially outperformed GPM IMERG. The Morrison scheme (103 mm/day) is close to GPM IMERG at the Mandi location, followed by WSM5 (102.93 mm/day) and WSM3 (117.04 mm/day). According to Fig. 4g, k, the Morrison and WSM5 schemes spatially overestimated the observed rainfall. The rest

of the schemes/experiments could not identify a significant proportion of the rain when transitioning from outer to inner domains.

Overall, we can infer that as we move from coarser to higher resolution, the WSM3 scheme is most consistent with GPM IMERG. However, the GPM IMERG and IMDAA were overestimated by the Morrison and WSM5 schemes. Furthermore, the other schemes could identify the most significant rainfall west of the Mandi location. As a result, we can conclude that the WSM3 scheme could capture the high rainfall event in terms of quantity and spatial distribution throughout the study region.

3.2 Bias in the simulated rainfall concerning the best scheme

As shown in Figs. 3 and 4, the WSM3 is a substantially better scheme for capturing the high rainfall event in the study region. As a response, we have used this scheme to compute the bias for the model simulations using the other schemes. The bias in rainfall amount in the
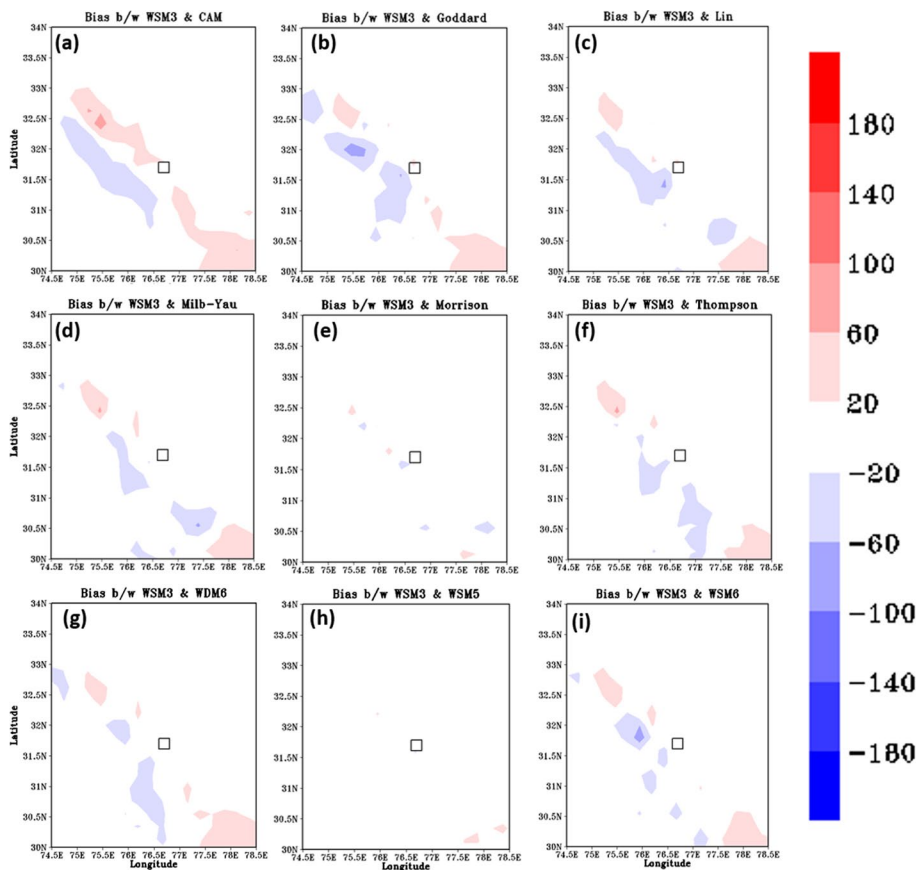
Fig. 5 Bias (mm/day) in precipitation of the outer domain valid for 24 h during August 07 2015 from the best model WSM3 with other parameterization schemes, i.e., **a** CAM, **b** Goddard, **c** Lin, **d** Milbrandt-Yau, **e** Morrison, **f** Thompson, **g** WDM6, **h** WSM5, and **i** WSM6. The box symbol represents the location of the Mandi (31.7°N, 76.7°E) region
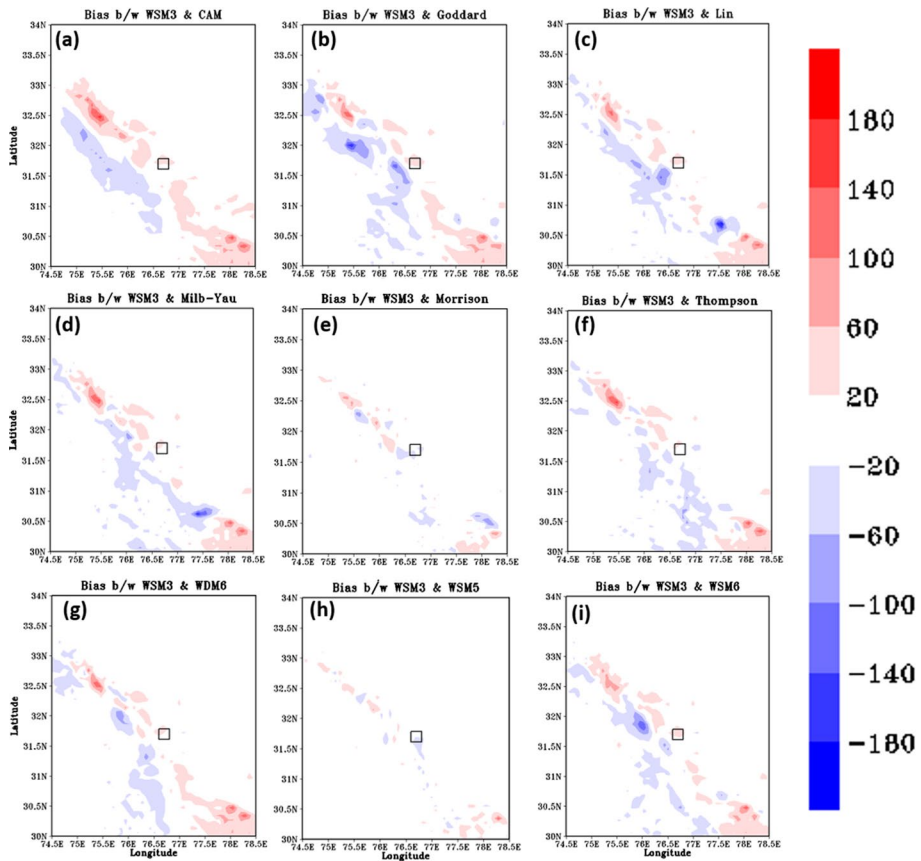
Fig. 6 Bias (mm/day) in precipitation of the inner domain valid for 24 h during August 07 2015 from the best model WSM3 with other parameterization schemes, i.e., **a** CAM, **b** Goddard, **c** Lin, **d** Milbrandt-Yau, **e** Morrison, **f** Thompson, **g** WDM6, **h** WSM5, and **i** WSM6. The box symbol represents the location of the Mandi (31.7°N, 76.7°E) region

different schemes concerning the WSM3 has been estimated geographically for the outer (1st) and inner (2nd) domains, respectively, in Figs. 5 and 6. Figures 5 and 6 show that the Morrison and WSM5 schemes are reasonably similar to the WSM3. It is also noted that the WSM3 underestimates the other schemes (Fig. 5) in Mandi's west-south region, whereas the WSM3 underestimates and overestimates the other schemes (Fig. 6) in the Mandi location's west-south region and diagonal region, respectively. Overall, we can conclude that when we assess from coarser to higher resolution, Morrison and WSM5 schemes are very close to the WSM3.

3.3 Explanation of the rainfall patterns with various meteorological parameters

3.3.1 Simulation of cloud fraction

The fraction of low, mid, and high clouds from all the experiments have been illustrated in Figs. 7–9. It is defined as a proportion of the cloud cover over a grid box indicating the tiny
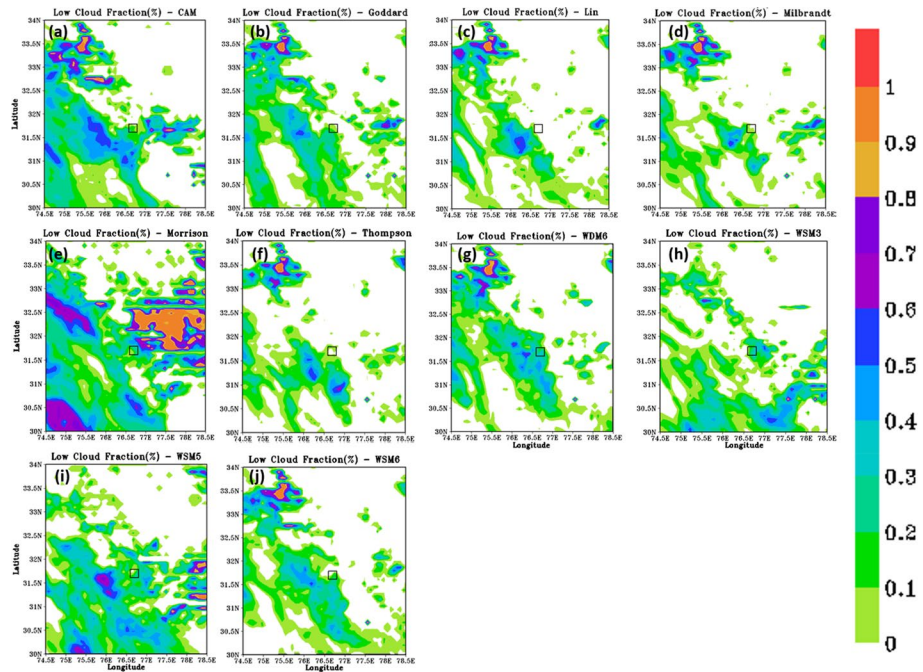
Fig. 7 Low cloud fraction (%) of the inner domain valid for 24 h on August 07 2015 with different parameterization schemes, i.e., **a** CAM, **b** Goddard, **c** Lin, **d** Milbrandt-Yau, **e** Morrison, **f** Thompson, **g** WDM6, **h** WSM3, **i** WSM5, and **j** WSM6. The box symbol represents the location of the Mandi (31.7°N, 76.7°E) region

droplets and/or ice particles in the lower and mid atmosphere. A cloud percentage of 1 signifies that the pixel is entirely clouded, whereas a cloud percentage of zero means the pixel is cloudless (Chen et al. 2012). The colors of clouds vary from green (no clouds) to red (clouds maxima). The high, mid, and low clouds form above the earth's surface at 6000 m, 2000 m, and 300 m, respectively.

It is shown from Fig. 7 that the formation of low cloud fraction is most significant in the Morrison scheme, followed by WSM3 and CAM over the study region. On the other hand, the Lin and Thompson schemes exhibited a smaller fraction of low clouds. It can also be observed that the Morrison, CAM, and WSM5 schemes encountered a large fraction of clouds spatially in their respective regions. In addition, the analysis of Fig. 8 reveals that establishing a mid-level cloud cover percentage/fraction occurs more often in the Morrison scheme spatially. Both the WSM3 and the WSM5 experiments cannot identify the spatial distribution of cloud cover. Except for Morrison, WSM3, and WSM5, all schemes have shown considerable mid-cloud cover to the northwest of the Mandi region. The high cloud cover fraction is computed for each of the schemes, and the results are shown in Fig. 9. It has been seen that the probability of a heavy high cloud cover forming in the Morrison scheme is substantial over the Mandi area along with some other locations. In addition, it can be observed that all of the schemes, except CAM and Morrison, have shown a significant amount of heavy high cloud cover to the southeast of the Mandi location. Thus, it can be concluded that spatially, the probability of low, mid, and high cloud cover formation is prominent in the Morrison scheme.
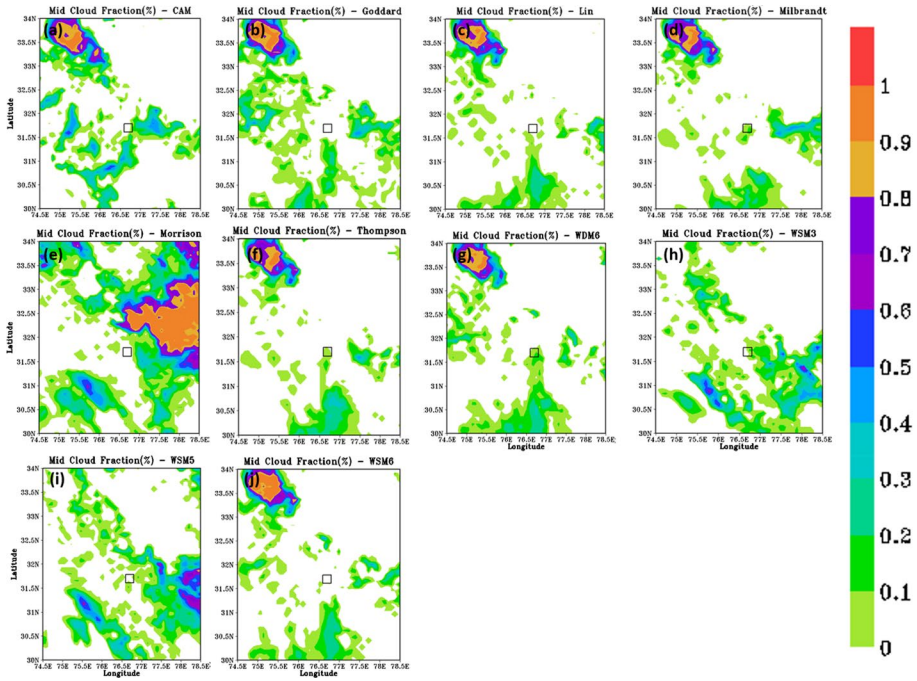
Fig. 8 Mid-level cloud fraction (%) of the inner domain valid for 24 h on August 07 2015 with different parameterization schemes, i.e., **a** CAM, **b** Goddard, **c** Lin, **d** Milbrandt-Yau, **e** Morrison, **f** Thompson, **g** WDM6, **h** WSM3, **i** WSM5, and **j** WSM6. The box symbol represents the location of the Mandi (31.7°N, 76.7°E) region

3.3.2 Simulation of cloud reflectivity and hydrometeor

The reflectivity measures the amount of solar radiation reflectance due to the cloud bands. A large reflectivity distribution indicates the presence of clouds that may generate rainfall. The maximum reflectivity of the inner domain is plotted for ten experiments (provided in Table 3), as can be seen in Fig. 10. It has been noticed that the Morrison scheme displays the maximum reflectivity of radiations over the domain, followed by the WSM5 scheme. If we compare all the schemes, a large proportion of cloud reflectance was seen to the west of the Mandi location, except for WSM3 and WSM5. The WSM3 and WSM5 schemes indicated the maximum reflectivity when looking southeast from the HRE location. The model simulations denote that the Morrison scheme showed the highest possible reflectivity across the domain.

Figure 11 displays the vertical profile of model simulated hydrometeor water vapor mixing ratio (Qvapor; unit: Kg/Kg) from the experiments related to the CMP schemes (CAM, Goddard, Lin, Milbrandt–Yau, Morrison, Thompson, WDM6, WSM3, WSM5, and WSM6) over the study region valid for 07 August 2015. Qvapor is the ratio of the mass of water vapor to the mass of dry air in a given volume in the atmosphere. The behavior of the model simulations was more or less similar for all the schemes as they showed a gradual decrease of the Qvapor (~0.018 to ~0.001 kg/Kg)) from the lower troposphere to the mid-troposphere (500 to 400 hPa). In the lower atmosphere,
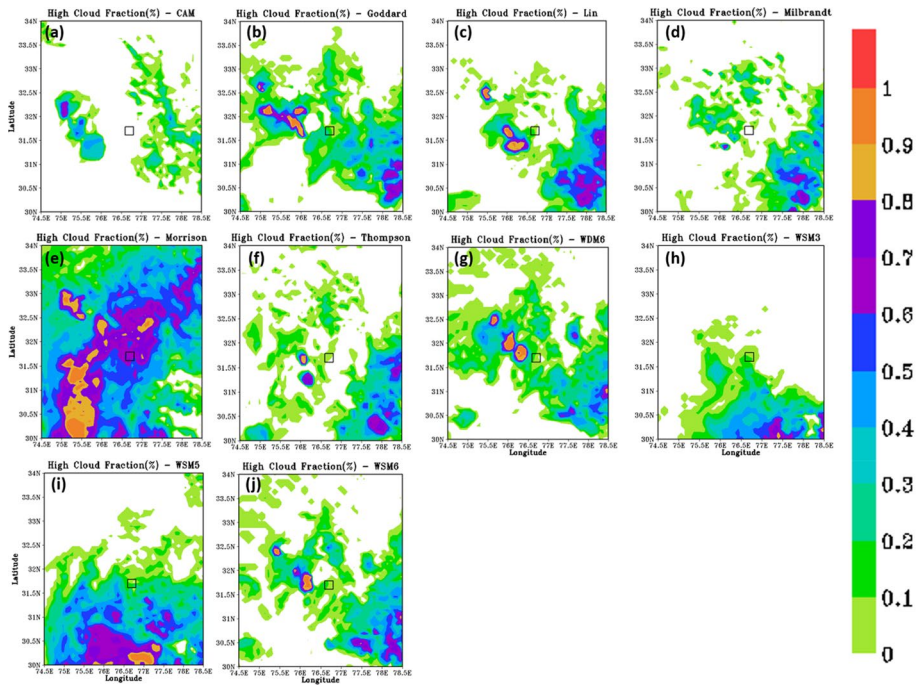
Fig. 9 High cloud fraction (%) of the inner domain valid for 24 h on August 07 2015 with different parameterization schemes, i.e., **a** CAM, **b** Goddard, **c** Lin, **d** Milbrandt-Yau, **e** Morrison, **f** Thompson, **g** WDM6, **h** WSM3, **i** WSM5, and **j** WSM6. The box symbol represents the location of the Mandi (31.7°N, 76.7°E) region

simulations with CAM and WSM5 schemes produced relatively lesser values than others.

3.3.3 Simulation of maximum convective available potential energy (MCAPE)

Figure 12 depicts the simulated MCAPE (J/kg) from all experiments for the inner domain. The figure shows that Milbrandt-Yau, Thompson, WSM6, and Lin have the highest MCAPE values across the domain. Furthermore, the MCAPE value for the Mandi location is relatively high (up to 1016.82 J/kg) in the Milbrandt scheme, followed by Thompson (889.32 J/kg). The MCAPE values for the CAM, Morrison, WSM3, and WSM5 schemes were relatively lower. The figure further demonstrates the Thompson, Milbrandt-Yau, Lin, and WSM6 schemes have a high value of MCAPE in the southwest of the study location. Overall, the Thompson and Milbrandt-Yau schemes showed maximum potential to perform the convection process over the domain.

3.3.4 Simulation of wind patterns at 850 hPa

The wind flow field is analyzed for the inner domain for all the schemes at 850 hPa. The results are shown in Fig. 13. All the schemes have the wind flow field located in the south and southwest of the domain only due to the high altitude in the north and northeast
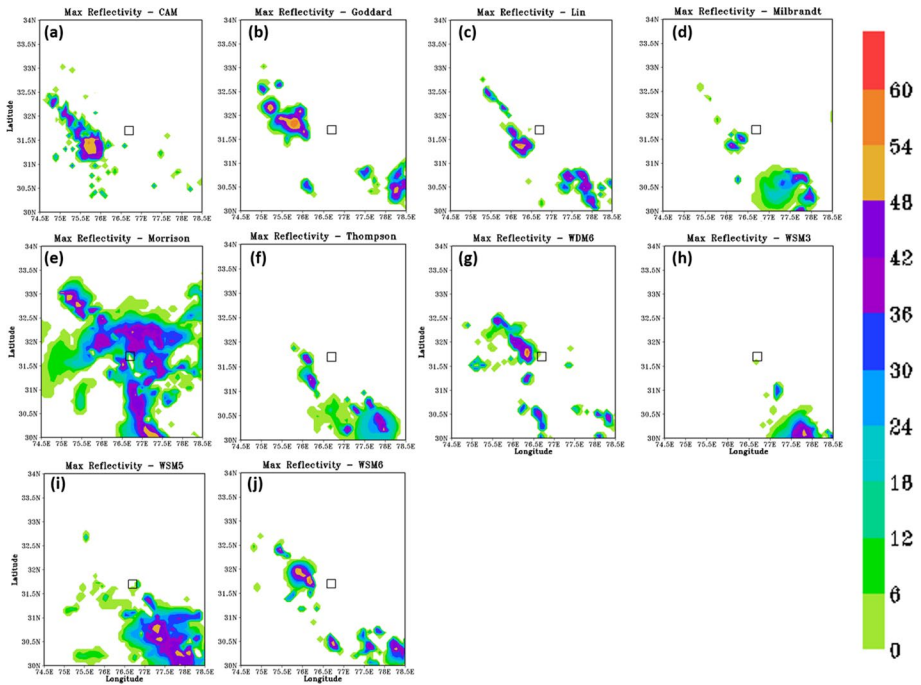
Fig. 10 Maximum reflectivity (dBZ) of the inner domain valid for 24 h on August 07 2015 with different parameterization schemes i.e., **a** CAM, **b** Goddard, **c** Lin, **d** Milbrandt-Yau, **e** Morrison, **f** Thompson, **g** WDM6, **h** WSM3, **i** WSM5, and **j** WSM6. The box symbol represents the location of the Mandi (31.7°N, 76.7°E) region

regions. The wind flow field over the study area showed a consistent pattern throughout in Fig. 13a–d, f, g, as well as (j). The Morrison, WSM3, and WSM5 schemes produced the same wind flow pattern with a speed of 10 m/s. In addition, it can be noted that the wind speed is low on the periphery of the Mandi region; however, the wind flow is vital in the western part of it and blows in a direction that is parallel to the x-axis and in the southeast direction. Aside from that, every other experiment had the same wind pattern but an abrupt and quick bend toward the north direction. Overall, the wind flow pattern is more or less similar in Morrison, WSM3, and WSM5 schemes throughout the domain, with a magnitude of 10 m/s.

4 Summary

In this study, the high-resolution Weather Research and Forecasting (WRF) model simulated a heavy rainfall event (HRE) over the Mandi region (31.7°N, 76.7°E) on August 07 2015. The Mandi is located in the Himachal Pradesh state of India at an elevation of 760 m from mean sea level. This weather system was quite severe regarding precipitation/rainfall, highlighted and reported by the Indian Meteorological Department and top-level national–international media. To analyze its various characteristics, we have simulated this event by performing the sensitivity experiments with ten cloud microphysics
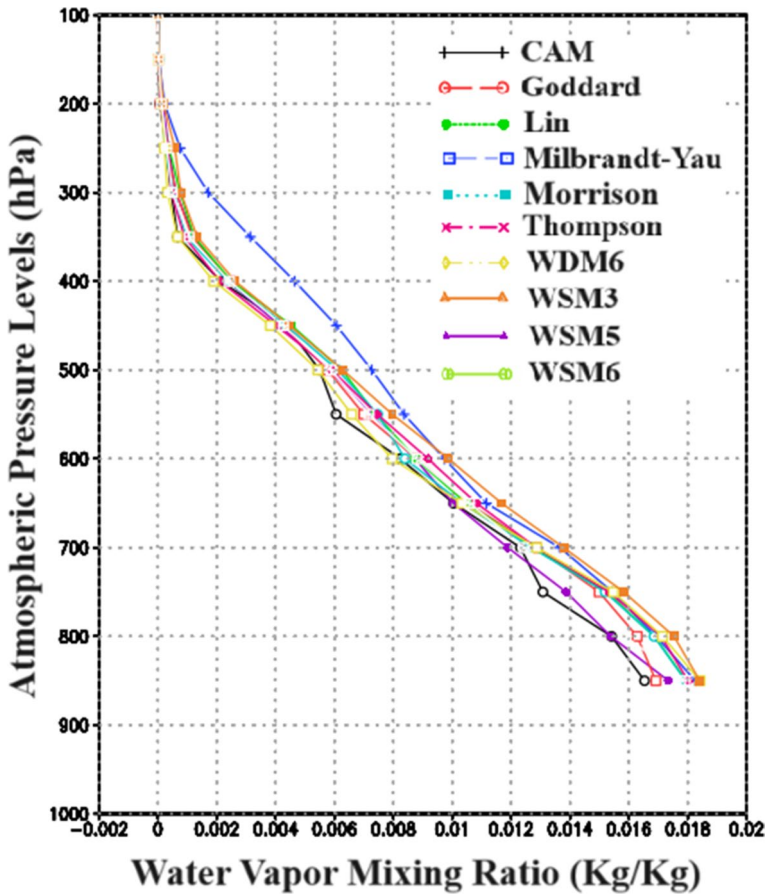
Fig. 11 Vertical profile of simulated water vapor mixing ratio (Kg/Kg) valid for 07 August 2015 over the Mandi, India

parameterization schemes, as discussed in Tables 2 and 3. The high-resolution and globally accepted reanalysis and satellite-based precipitation products IMDAA and GPM IMERG have been used as a proxy for the observation to validate the model outputs. We have evaluated this event by taking two nested domains on which lateral boundary and initial conditions have been incorporated. These conditions are taken from NCEP with $0.25° \times 0.25°$ horizontal and six hourly temporal resolutions.

It was found that when we move from coarser to higher resolution (or outer to inner domain), the WSM3 scheme/experiment is the sole one that is most consistent with GPM IMERG. However, the GPM IMERG and IMDAA were overestimated by the Morrison and WSM5 schemes. Furthermore, the other schemes could identify the maximum
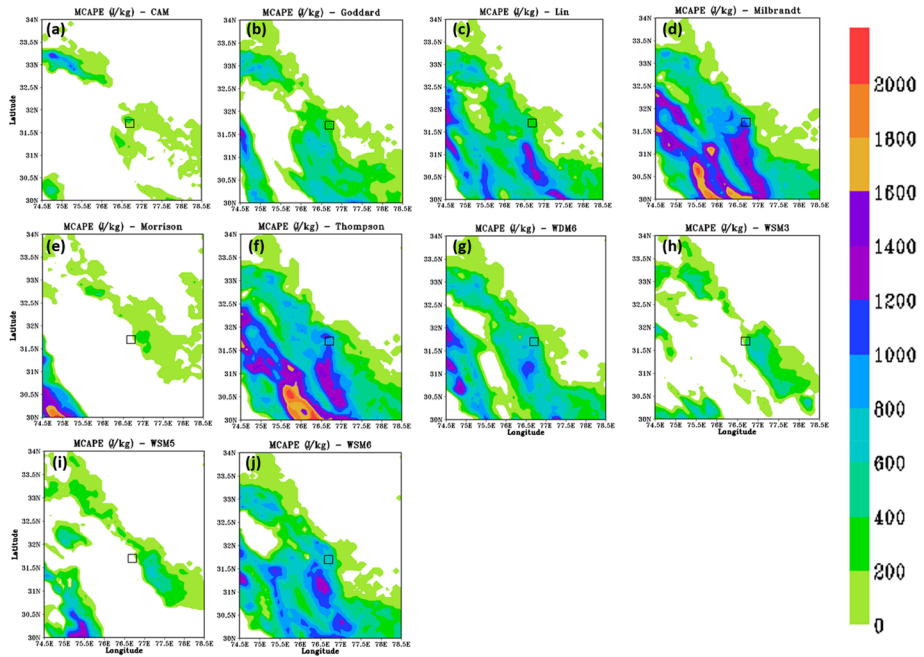
Fig. 12 Maximum Convective Potential Energy (MCAPE) (J/kg) of the inner domain valid for 24 h during August 07 2015 with different parameterization schemes i.e., **a** CAM, **b** Goddard, **c** Lin, **d** Milbrandt-Yau, **e** Morrison, **f** Thompson, **g** WDM6, **h** WSM3, **i** WSM5, and **j** WSM6. The box symbol represents the location of the Mandi (31.7°N, 76.7°E) region

rain proportion to the Mandi location's west. Therefore, the WSM3 scheme could capture the high rainfall event in terms of quantity and spatial distribution throughout the study region. Furthermore, the bias in simulated rainfall distribution is evaluated for both domains using all the schemes concerning WSM3. When we assess from coarser to higher resolution, Morrison and WSM5 schemes are very close to the WSM3. Moreover, other meteorological parameters are evaluated, such as cloud fraction, maximum reflectivity due to clouds, MCAPE, and wind flow field associated with rainfall patterns. The probability of low, mid, and high cloud cover formation was prominent in the Morrison scheme. Also, the Morrison scheme showed the highest possible reflectivity across the domain. In contrast, MCAPE was evaluated across the domain, and it was concluded that the Thompson and Milbrandt-Yau schemes showed maximum potential to perform the convection process over the domain. Apart from this, the wind patterns are also evaluated at 850 hPa over the region. The wind flow pattern was more or less similar in Morrison, WSM3, and WSM5 schemes throughout the domain, with a magnitude of 10 m/s.
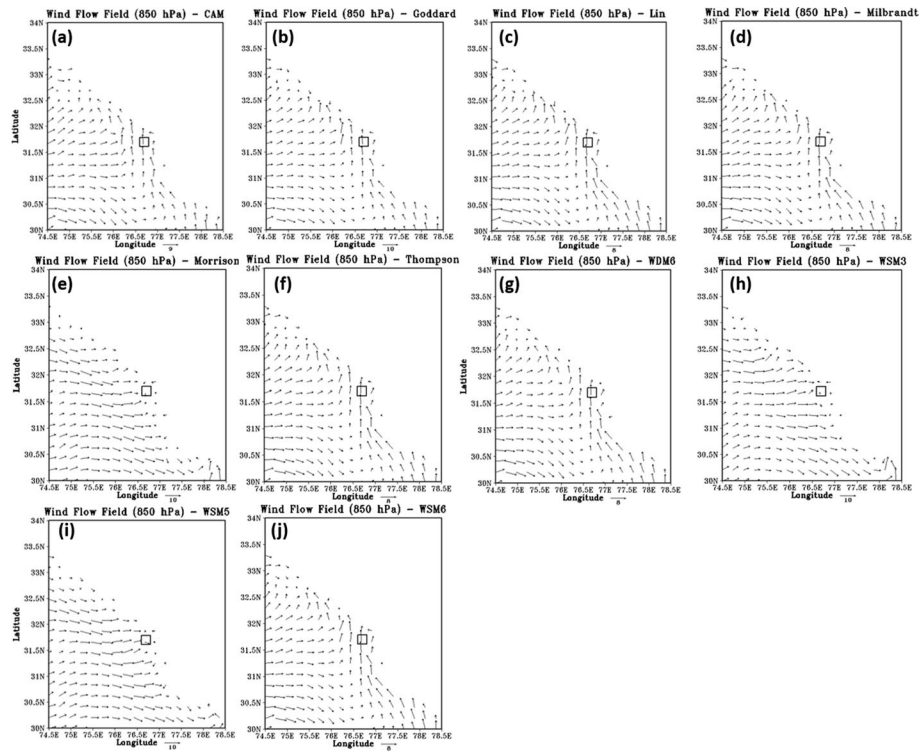
Fig. 13 Wind flow field (m/s) of the inner domain valid for 24 h during August 07 2015 with different parameterization schemes i.e., **a** CAM, **b** Goddard, **c** Lin, **d** Milbrandt-Yau, **e** Morrison, **f** Thompson, **g** WDM6, **h** WSM3, **i** WSM5, and **j** WSM6 at 850 hPa. The box symbol represents the location of the Mandi (31.7°N, 76.7°E) region

Data availability The data used in this study include NCEP-NCAR, GFS, GPM IMERG, and IMDAA data sets that are all free.

Code availability In this study, the WRF model is used for simulations. This model is accessible with open-source licenses.

Declarations

Conflict of interest The authors declare that they have no conflict of interest.

Ethical approval All authors approve.

Consent to participate All authors agreed with the content, all gave explicit consent to submit, and they obtained consent from the responsible authorities at the institute/organization where the work has been carried out, before the work is submitted.

References

Ashrit R, Indira Rani S, Kumar S, Karunasagar S, Arulalan T, Francis T, Routray A, Lasker SI, Mahmood S, Jermey P, Maycock A, Renshaw R, George JP, Rajagopal EN (2020) IMDAA regional reanalysis: Performance evaluation during Indian summer monsoon season. J Geophys Res Atmos 125:1–26

Bharti V (2015) Investigation of extreme rainfall events over the Northwest Himalaya region using satellite data (Master's thesis, University of Twente).

Chen SH, Sun WY (2002) A one-dimensional time-dependent cloud model. J Meteorol Soc Japan 80:99–118

Chen L, Yan G, Wang T, Ren H, Calbó J, Zhao J, McKenzie R (2012) Estimation of surface shortwave radiation components under all-sky conditions: modeling and sensitivity analysis. Remote Sens Environ 123:457–469

Chevuturi A, Dimri AP, Das S, Kumar A, Niyogi D (2015) Numerical simulation of an intense precipitation event over Rudraprayag in the central Himalayas during 13–14 September 2012. J Earth Syst Sci 124:1545–1561

Das S, Ashrit R, Moncrieff MW (2006) Simulation of a Himalayan cloudburst event. J Earth Syst Sci 115:299–313

Devi U, Shekhar MS, Singh GP (2021) Correction of mesoscale model daily precipitation data over Northwestern Himalaya. Theor Appl Climatol 143:51–60

Dimri AP, Chevuturi A, Niyogi D, Thayyen RJ, Ray K, Tripathi SN, Pandey AK, Mohanty UC (2017) Cloudbursts in Indian Himalayas: a review. Earth Sci Rev 168:1–23

Dudhia J (1989) Numerical study of convection observed during the winter monsoon experiment using a mesoscale two-dimensional model. J Atmos Sci 46:3077–3107

Eaton B (2011) User's guide to the community atmosphere model CAM-5.1. 1. NCAR.

Hong SY, Lim JOJ (2006) The WRF single-moment 6-class microphysics scheme (WSM6). Asia-Pac J Atmos Sci 42:129–151

Hong SY, Dudhia J, Chen SH (2004) A revised approach to ice microphysical processes for the bulk parameterization of clouds and precipitation. Mon Weather Rev 132:103–120

Hong SY, Noh Y, Dudhia J (2006) A new vertical diffusion package with an explicit treatment of entrainment processes. Mon Weather Rev 134:2318–2341

Huffman GJ, Bolvin DT, Nelkin EJ, Stocker EF, Tan J (2019) V06 IMERG release notes. NASA/GSFC: Greenbelt

Jena P, Garg S, Azad S (2020) Performance analysis of IMD high-resolution gridded rainfall (0.25°× 0.25°) and satellite estimates for detecting cloudburst events over the Northwest Himalayas. J Hydrometeorol 21:1549–1569

Jiménez PA, Dudhia J, González-Rouco JF, Navarro J, Montávez JP, García-Bustamante E (2012) A revised scheme for the WRF surface layer formulation. Mon Weather Rev 140:898–918

Kain JS (2004) The Kain-Fritsch convective parameterization: an update. J Appl Meteorol 43:170–181

Karki R, Gerlitz L, Schickhoff U, Scholten T, Böhner J (2017) Quantifying the added value of convection-permitting climate simulations in complex terrain: a systematic evaluation of WRF over the Himalayas. Earth Syst Dyn 8:507–528

Karki R, ul-Hasson S, Gerlitz L, Talchabhadel R, Schenk E, Schickhoff U, Scholten T, Böhner J (2018) WRF-based simulation of an extreme precipitation event over the Central Himalayas: atmospheric mechanisms and their representation by microphysics parameterization schemes. Atmos Res 214:21–35

Khadke L, Pattnaik S (2021) Impact of initial conditions and cloud parameterization on the heavy rainfall event of Kerala (2018). Model Earth Syst Environ 7:2809–2822

Kumar S, Routray A, Tiwari G, Chauhan R, Jain I (2017) Simulation of tropical cyclone 'Phailin'Using WRF modeling system. In: Tropical cyclone activity over the north Indian Ocean (pp. 307–316). Springer, Cham.

Lim KSS, Hong SY (2010) Development of an effective double-moment cloud microphysics scheme with prognostic cloud condensation nuclei (CCN) for weather and climate models. Mon Weather Rev 138:1587–1612

Milbrandt JA, Yau MK (2005a) A multi-moment bulk microphysics parameterization. Part I: Analysis of the role of the spectral shape parameter. J Atmos Sci 62:3051–3064

Milbrandt JA, Yau MK (2005b) A multi-moment bulk microphysics parameterization. Part II: a proposed three-moment closure and scheme description. J Atmos Sci 62:3065–3081

Mlawer EJ, Taubman SJ, Brown PD, Iacono MJ, Clough SA (1997) Radiative transfer for inhomogeneous atmospheres: RRTM, a validated correlated-k model for the longwave. J Geophys Res Atmos 102:16663–16682

Mohan M, Bhati S (2011) Analysis of WRF model performance over the subtropical region of Delhi, India. Adv Meteorol

Morrison H, Thompson G, Tatarskii V (2009) Impact of cloud microphysics on the development of trailing stratiform precipitation in a simulated squall line: Comparison of one-and two-moment schemes. Mon Weather Rev 137:991–1007

Patil R, Pradeep Kumar P (2016) WRF model sensitivity for simulating intense western disturbances over northwest India. Model Earth Syst Environ 2:1–15

Pegahfar N, Gharaylou M, Shoushtari MH (2022) Assessing the performance of the WRF model cumulus parameterization schemes for the simulation of five heavy rainfall events over the Pol-Dokhtar, Iran during 1999–2019. Nat Hazards, pp 1–27

Raghavan K (1973) Break-monsoon over India. Mon Weather Rev 101:33–43

Rajeevan M, Unnikrishnan CK, Bhate J, Niranjan Kumar K, Sreekala PP (2012) Northeast monsoon over India: variability and prediction. Meteorol Appl 19:226–236

Raju PVS, Mohanty UC, Bhatla R (2005) Onset characteristics of the southwest monsoon over India. Int J Climatol 25:167–182

Ramage CS (1971) Monsoon Meteorol No. 551.518 R3.

Shekhar MS, Chand H, Kumar S, Srinivasan K, Ganju A (2010) Climate-change studies in the western Himalaya. Ann Glaciol 51:105–112

Singh RB, Mal S (2014) Trends and variability of monsoon and other rainfall seasons in Western Himalaya, India. Atmos Sci Lett 15:218–226

Skamarock WC, Klemp JB, Dudhia J, Gill DO, Liu Z, Berner J, Wang W, Powers JG, Duda MG, Barker DM, Huang XY (2019) A description of the advanced research WRF model version 4. National Center for Atmospheric Research: Boulder, CO, USA

Sravana Kumar M, Shekhar MS, Rama Krishna SSVS, Bhutiyani MR, Ganju A (2012) Numerical simulation of cloud burst event on August 05, 2010, over Leh using WRF mesoscale model. Nat Hazards 62:1261–1271

Tao WK, Simpson J, McCumber M (1989) An ice-water saturation adjustment. Mon Weather Rev 117:231–235

Tao WK, Wu D, Lang S, Chern JD, Peters-Lidard C, Fridlind A, Matsui T (2016) High-resolution NU-WRF simulations of a deep convective-precipitation system during MC3E: Further improvements and comparisons between Goddard microphysics schemes and observations. J Geophys Res Atmos 121:1278–1305

Tewari M, Chen F, Wang W, Dudhia J, LeMone MA, Ek K, Mitchell M, Gayno G, Wegiel J, Cuenca RH (2004) Implementation and verification of the unified NOAH land surface model in the WRF model. In: 20th conference on weather analysis and forecasting/16th conference on numerical weather prediction, vol 14, pp 2165–2170

Thompson G, Rasmussen RM, Manning K (2004) Explicit forecasts of winter precipitation using an improved bulk microphysics scheme. Part I: description and sensitivity analysis. Mon Weather Rev 132:519–542

Thompson G, Field PR, Rasmussen RM, Hall WD (2008) Explicit forecasts of winter precipitation using an improved bulk microphysics scheme. Part II: implementation of a new snow parameterization. Mon Weather Rev 136:5095–5115

Tiwari G, Kumar P (2022) Predictive skill comparative assessment of WRF 4DVar and 3DVar data assimilation: an Indian Ocean tropical cyclone case study. Atmos Res. https://doi.org/10.1016/j.atmosres.2022.106288

Tiwari G, Kumar P (2023) Four-dimensional ensemble-variational (4DEnVar) data assimilation of satellite radiance using WRF model for the prediction of north Indian Ocean tropical cyclones. Adv Space Res. https://doi.org/10.1016/j.asr.2023.03.015

Tiwari G, Kumar S, Routray A, Panda J, Jain I (2019) A high-resolution mesoscale model approach to reproduce super typhoon Maysak (2015) over Northwestern Pacific Ocean. Earth Syst Environ 3:101–112

Tiwari G, Kumar P, Mishra AK (2022) Effect of background error tuning on assimilating satellite radiance: evidence for the prediction of tropical cyclone track and intensity. In 18th Annual Meeting of the Asia Oceania Geosciences Society: Proceedings of the 18th annual meeting of the Asia Oceania Geosciences Society (AOGS 2021), pp 4–6

Vellore RK, Kaplan ML, Krishnan R, Lewis JM, Sabade S, Deshpande N, Singh BB, Madhura RK, Rama Rao MVS (2016) Monsoon-extratropical circulation interactions in Himalayan extreme rainfall. Clim Dyn 46:3517–3546